



1 **Applicability of physics-based and machine-learning-based algorithms of**
2 **geostationary satellite in retrieving the diurnal cycle of cloud base height**

3

4 Mengyuan Wang¹, Min Min^{1*}, Jun Li², Han Lin³, Yongen Liang¹, Binlong Chen²,
5 Zhigang Yao⁴, Na Xu², Miao Zhang²

6

7

8 ¹School of Atmospheric Sciences, Southern Marine Science and Engineering
9 Guangdong Laboratory (Zhuhai), and Guangdong Province Key Laboratory for
10 Climate Change and Natural Disaster Studies, Zhuhai 519082, China

11 ²Key Laboratory of Radiometric Calibration and Validation for Environmental
12 Satellites and Innovation Center for FengYun Meteorological Satellite (FYSIC),
13 National Satellite Meteorological Center (National Center for Space Weather), China
14 Meteorological Administration, Beijing 100081, China

15 ³Key Laboratory of Spatial Data Mining and Information Sharing of Ministry of
16 Education, National and Local Joint Engineering Research Center of Satellite
17 Geospatial Information Technology, Fuzhou University, Fuzhou 350108, China

18 ⁴Beijing Institute of Applied Meteorology, Beijing 100029, China

19

20

21

22 *Correspondence to:* Min Min (minm5@mail.sysu.edu.cn)

23

24

25

26

27

28

29

30

31

32

33



34 **Abstract.** Four distinct retrieval algorithms, comprising two physics-based and two
35 machine-learning (ML) approaches, have been developed to retrieve cloud base
36 height (CBH) and its diurnal cycle from Himawari-8 geostationary satellite
37 observations. Validations have been conducted using the joint CloudSat/CALIOP
38 (Cloud-Aerosol Lidar with Orthogonal Polarization) CBH products in 2017, ensuring
39 independent assessments. Results show that the two ML-based algorithms exhibit
40 markedly superior performance (with a correlation coefficient of $R > 0.91$ and an
41 absolute bias of approximately 0.8 km) compared to the two physics-based algorithms.
42 However, validations based on CBH data from the ground-based lidar at the Lijiang
43 station in Yunnan province and the cloud radar at the Nanjiao station in Beijing,
44 China, explicitly present contradictory outcomes ($R < 0.60$). An identifiable issue
45 arises with significant underestimations in the retrieved CBH by both ML-based
46 algorithms, leading to an inability to capture the diurnal cycle characteristics of CBH.
47 The strong consistence observed between CBH derived from ML-based algorithms
48 and the spaceborne active sensor may be attributed to utilizing the same dataset for
49 training and validation, sourced from the CloudSat/CALIOP products. In contrast, the
50 CBH derived from the optimal physics-based algorithm demonstrates the good
51 agreement in diurnal variations of CBH with ground-based lidar/cloud radar
52 observations during the daytime (with an R value of approximately 0.7). Therefore,
53 the findings in this investigation from ground-based observations advocate for the
54 more reliable and adaptable nature of physics-based algorithms in retrieving CBH
55 from geostationary satellite measurements. Nevertheless, under ideal conditions, with
56 an ample dataset of spaceborne cloud profiling radar observations encompassing the
57 entire day for training purposes, the ML-based algorithms may hold promise in still
58 delivering accurate CBH outputs.

59 **Key words:** Geostationary meteorological satellite; cloud base height; physics-based
60 algorithm; machine learning.

61



62 **1 Introduction**

63 Clouds, comprising visible aggregates like atmospheric water droplets,
64 supercooled water droplets, ice crystals, etc., blanket roughly 70% of the Earth's
65 surface (Stubenrauch et al., 2013). They play a pivotal role in global climate change,
66 the hydrometeor cycle, aviation safety, and serve as a primary focus in weather
67 forecasting and climate research, particularly storm clouds (Hansen, 2007; Hartmann
68 and Larson, 2002). From advanced geostationary (GEO) and polar-orbiting (LEO,
69 low earth orbit) satellite imagers, various measurable cloud properties, such as
70 fraction, phase, top height, and optical depth, are routinely retrieved. However, the
71 high-quality cloud geometric height (CGH) and CBH, a fundamental macro physical
72 parameter delineating the vertical distribution of clouds, remains relatively
73 understudied and underreported. Nonetheless, for boundary-layer clouds, the cloud
74 base height stands as a critical parameter influencing other cloud-controlling variables.
75 These variables encompass the cloud-base temperature (Zhu et al., 2014), cloud-base
76 vertical velocity (Zheng et al., 2020), activation of CCN (Cloud Condensation Nuclei)
77 at the cloud-base (Rosenfeld et al., 2016; Miller et al., 2023), and the cloud-surface
78 decoupling state (Su et al., 2022). These factors significantly impact convective cloud
79 development and ultimately the climate. Hence, the accurate determination of CBH
80 and its diurnal cycle with high spatial-temporal resolution becomes very important,
81 necessitating comprehensive investigations (Viúdez-Mora et al., 2015; Wang et al.,
82 2020). Such efforts can provide deeper insights into potential ramifications of cloud
83 on radiation equilibrium and global climate systems.

84 However, as one of the most crucial cloud physical parameters in atmospheric
85 physics, the CBH poses challenges in terms of measurement or estimation from space.
86 Presently, the primary methods for measuring CBH rely on ground-based
87 observations, utilizing tools such as sounding balloons, Mie-scattering lidars,
88 stereo-imaging cloud-height detection technologies, and cloud probe sensors
89 (Forsythe et al., 2000; Hirsch et al., 2011; Seaman et al., 2017; Zhang et al., 2018;
90 Zhou et al., 2019; Zhou et al., 2024). While *in-situ* ground-based observation methods
91 offer highly accurate, reliable, and timely continuous CBH results, they are
92 constrained by localized observation coverage and the sparse distribution of
93 observation sites (Aydin and Singh, 2004). In recent decades, with the rapid



94 advancement of meteorological satellite observation technology, spaceborne
95 observing methods have emerged that provide global cloud observations with high
96 spatio-temporal resolution compared to conventional ground-based remote sensing
97 methods. In this realm, satellite remote sensing techniques for measuring CBH fall
98 primarily into two categories: active and passive methods. Advanced active remote
99 sensing technologies like CloudSat and Cloud-Aerosol Lidar and Infrared Pathfinder
100 Satellite Observation (CALIPSO) in the National Aeronautics and Space
101 Administration (NASA) A-Train series can capture global cloud profiles, including
102 CBH, with high quality by detecting unique return signals from cloud layers using
103 onboard active millimeter wave radar or lidar. However, their viewing footprints are
104 limited along the nadir of the orbit, implying that observation coverage remains
105 confined primarily to a horizontal scale (Min et al., 2022; Lu et al., 2021).

106 In addition to active remote sensing methods, satellite-based passive remote
107 sensing technologies can also play an important role in estimating CBH (Meerkötter
108 and Bugliaro, 2009; Lu et al., 2021). As well known, the physics-based principles and
109 retrieval methods for cloud top height (CTH) have reached maturity and are now
110 widely employed in satellite passive remote sensing field (Heidinger and Pavolonis,
111 2009; Wang et al., 2022). However, the corresponding physical principles or methods
112 for measuring CBH using satellite passive imager measurements are still not entirely
113 clear and unified (Heidinger et al., 2019; Min et al., 2020). A recent study by (Yang et
114 al., 2021) utilized oxygen A-band data observed by the Orbiting Carbon Observatory
115 2 (OCO-2) to retrieve single-layer marine liquid CBH. Two primary methods are
116 prominent in retrieving CBH through passive space-based remote sensing techniques.
117 The first method involves the extrapolation technique for retrieving CBH for clouds
118 of the same type. For instance, (Wang et al., 2012) proposed a method to extrapolate
119 CBH from CloudSat using spatial-temporally matched MODIS (Moderate Resolution
120 Imaging Spectroradiometer) cloud classification data. The second physics-based
121 retrieval method first approximates the cloud geometric thickness using its optical
122 thickness. It then employs the previously derived CTH product to compute the
123 correlated CBH using the respective NOAA (National Oceanic and Atmospheric
124 Administration) SNPP/VIIRS (Suomi National Polar-orbiting Partnership/Visible
125 Infrared Imaging Radiometer Suite) products (Noh et al., 2017). Hutchison et al. also
126 formulated an empirical algorithm that estimates both cloud geometric thickness and
127 CBH. This algorithm relies on statistical analyses derived from MODIS cloud optical



128 thickness and cloud liquid water path products (Hutchison et al., 2006; Hutchison,
129 2002).

130 Machine learning (ML) has proven to be highly effective in addressing nonlinear
131 problems within remote sensing and meteorology fields, such as precipitation
132 estimation and CTH retrieval (Min et al., 2020; HåKansson et al., 2018; Kühnlein et
133 al., 2014). In recent years, several previous studies have leveraged ML-based
134 algorithms to retrieve CBH, establishing nonlinear connections between CBH and
135 GEO satellite observations. For instance, Tan et al. (2020) integrated CTH and cloud
136 optical properties products from Fengyun-4A (FY-4A) GEO satellite with
137 spatial-temporally matched CBH data from CALIPSO/CloudSat (Tan et al., 2020).
138 They developed a random forest (RF) model for CBH retrieval. Similarly, Lin et al.
139 (2022) constructed a gradient boosted regression tree (GBRT) model using U.S.
140 new-generation Geostationary Operational Environmental Satellites-R Series
141 (GOES-R) Advanced Baseline Imager (ABI) level 1B radiance data and the ERA5
142 (the fifth generation ECMWF) reanalysis dataset (Lin et al., 2022). They employed
143 CALIPSO CBH data as labels to achieve single-layer CBH retrievals. Notably, the
144 CBH quality of ML-based algorithms was found to surpass that of physics-based
145 algorithms (Lin et al., 2022). Moreover, Tana et al. (2023) utilized Himawari-8 data
146 and the random forest algorithm to develop a novel CBH algorithm, achieving a high
147 correlation coefficient of 0.92 and a low root mean square error (RMSE) of 1.17 km
148 (Tana et al., 2023).

149 However, these former studies did not discuss whether both physics-based and
150 ML-based algorithms of GEO satellite could retrieve the diurnal cycle of CBH well.
151 This gap in research could be mainly attributed to potential influences from the fixed
152 LEO satellite (with active radar or lidar) passing time in the previous CBH retrieval
153 model (Lin et al., 2022). As well known, there are distinct diurnal cycle
154 characteristics of clouds in different regions across the globe (Li et al., 2022). These
155 diurnal cycle characteristics primarily stem from the daily solar energy cycle absorbed
156 by both the atmosphere and Earth's surface. Besides, vertical atmospheric motions are
157 shaped by imbalances in atmospheric heating and surface configurations, also leading
158 to a range of cloud movements and structures (Miller et al., 2018). Hence, it is crucial
159 to thoroughly investigate the diurnal cycle features of CBH derived from GEO
160 satellite measurements by comparing them with ground-based radar and lidar
161 observations (Min and Zhang, 2014; Warren and Eastman, 2014). In this study, we



162 aim to assess the applicability and feasibility of both physics-based and ML-based
163 algorithms of GEO satellites in capturing the diurnal cycle characteristics of CBH.

164 The subsequent sections of this paper are structured as follows. Section 2
165 provides a concise overview of the data employed in this study. Following that,
166 section 3 introduces the four distinct physics/ML-based CBH retrieval algorithms. In
167 section 4, the CBH results obtained from these four algorithms are analyzed, and
168 comparisons are drawn with spatially and temporally matched CBHs from
169 ground-based cloud radar and lidar. Finally, section 5 encapsulates the primary
170 conclusions and new findings derived from this study.

171 **2 Data**

172 In this study, observations from the Himawari-8 (H8) Advanced Himawari
173 Imager (AHI) are utilized for the retrieval of high spatiotemporal resolution CBH.
174 Launched successfully by the Japan Meteorological Administration on October 7,
175 2014, the H8 geostationary satellite is positioned at 140.7°E. The AHI onboard H8
176 encompasses 16 spectral bands ranging from 0.47 μm to 13.3 μm , featuring spatial
177 resolutions of 0.5–2 km. This includes 3 visible (VIS) bands at 0.5–1 km, 3
178 near-infrared (NIR) bands at 1–2 km, and 10 infrared (IR) bands at 2 km. The
179 H8/AHI can scan a full disk area within 10 minutes, two specific areas within 2.5
180 minutes, a designated area within 2.5 minutes, and two landmark areas within 0.5
181 minutes (Iwabuchi et al., 2018). Its enhanced temporal resolution and observation
182 frequency facilitates the tracking of rapidly changing weather systems, enabling the
183 accurate determination of quantitative atmospheric parameters (Bessho et al., 2016).

184 Operational H8/AHI Level-1B data, accessible from July 7, 2015, are freely
185 available on the satellite product homepage of the Japan Aerospace Exploration
186 Agency (Letu et al., 2019). The Level-2 cloud products utilized in this study,
187 including cloud mask (CLM), CTH, cloud effective particle radius (CER), and cloud
188 optical thickness (COT), are generated by the Fengyun satellite science product
189 algorithm testbed (FYGAT) (Wang et al., 2019; Min et al., 2017) of the China
190 Meteorological Administration (CMA) for various applications. It is important to note
191 that certain crucial preliminary cloud products, such as the cloud mask, have been
192 validated in prior studies (Wang et al., 2019; Liang et al., 2023). Nevertheless, before
193 initiating CBH retrieval, it is imperative to validate the H8/AHI cloud optical and



194 microphysical products from the FYGAT retrieval system. This validation is carried
195 out by using analogous MODIS Level-2 cloud products as a reference. Additional
196 details regarding the validation of cloud products are provided in the Appendix A
197 section.

198 In addition to the H8/AHI Level-1/2 data, the Global Forecast System (GFS)
199 numerical weather prediction (NWP) data are employed for CBH retrieval in this
200 study. The variables include land/sea surface temperature and the vertical profiles of
201 temperature, humidity, and pressure. Operated by the U.S. NOAA (Kalnay et al.,
202 1996), the GFS serves as a global and advanced NWP system. The operational GFS
203 system routinely delivers globally high-quality and gridded NWP data at 3-hour
204 intervals, with four different initial forecast times per day (00:00, 06:00, 12:00, and
205 18:00 UTC). The three-dimensional NWP data cover the Earth in a $0.5^\circ \times 0.5^\circ$ grid
206 interval and resolve the atmosphere with 26 vertical levels from the surface (1000 hPa)
207 up to the top of the atmosphere (10 hPa).

208 As previously mentioned, the official MODIS Collection-6.1 Level-2 cloud
209 product Climate Data Records are utilized in this study to validate the H8/AHI cloud
210 products (CTH, CER, and COT) generated by the FYGAT system. MODIS sensors
211 are onboard NASA Terra and Aqua polar-orbiting satellites. Terra functions as the
212 morning satellite, passing through the equator from north to south at approximately
213 10:30 local time, while Aqua serves as the afternoon satellite, traversing the equator
214 from south to north at around 13:30 local time. As a successor to the NOAA
215 Advanced Very High Resolution Radiometer (AVHRR), MODIS features 36
216 independent spectral bands and a broad spectral range from $0.4 \mu\text{m}$ (VIS) to $14.4 \mu\text{m}$
217 (IR), with a scanning width of 2330 km and spatial resolutions ranging from 0.25 to
218 1.0 km. Recent studies (Baum et al., 2012; Platnick et al., 2017) have highlighted
219 significant improvements and collective changes in cloud top, optical, and
220 microphysical properties from Collection-5 to Collection-6.

221 In addition to the passive spaceborne imaging sensors mentioned above, the
222 CloudSat satellite, equipped with a 94-GHz active cloud profiling radar (CPR), holds
223 the distinction of being the first sun-synchronous orbit satellite specifically designed
224 to observe global cloud vertical structures and properties. It is part of the A-Train
225 (Afternoon-Train) series of satellites, akin to the Aqua satellite, launched and
226 operated by NASA (Heymsfield et al., 2008). CALIPSO (Cloud-Aerosol Lidar and
227 Infrared Pathfinder Satellite Observation) is another polar-orbiting satellite within the



228 A-Train constellation, sharing an orbit with CloudSat and trailing it by a mere 10–15
229 seconds. CALIPSO is the first satellite equipped with an active dual-channel
230 Cloud-Aerosol Lidar with Orthogonal Polarization (CALIOP) at 532 and 1064 nm
231 bands (Hunt et al., 2009). Both CloudSat and CALIPSO possess notable advantages
232 over passive spaceborne sensors due to the 94-GHz radar of CloudSat and the joint
233 return signals of lidar and radar on CALIPSO. These features enhance their sensitivity
234 to optically thin cloud layers and ensure strong penetration capability, resulting in
235 more accurate CTH and CBH detections compared to passive spaceborne sensors
236 (CAL_LID_L2_05kmCLay-Standard-V4-10). The joint cloud type products of
237 2B-CLDCLASS-LIDAR, derived from both CloudSat and CALIPSO measurements,
238 offer a comprehensive description of cloud vertical structure characteristics, cloud
239 type, CTH, CBH, etc. The time interval between each profile in this product is
240 approximately 3.1 seconds, and the horizontal resolution is 2.5 km (along track)×1.4
241 km (cross-track). Each profile is divided into 125 layers with a 240-m vertical interval.
242 For more details on 2B-CLDCLASS-LIDAR products, please refer to the CloudSat
243 official product manual (Sassen and Wang, 2008).

244 **3 Physics/machine-learning based cloud-base height algorithms**

245 **3.1 GEO Cloud-base height retrieval algorithm from the interface data processing** 246 **segment of the Visible Infrared Imaging Radiometer Suite**

247 The Joint Polar Satellite System (JPSS) program is a collaborative effort between
248 NASA and NOAA. The operational CBH retrieval algorithm, part of the 30
249 Environmental Data Records (EDR) of JPSS, can be implemented operationally
250 through the Interface Data Processing Segment (IDPS) (Baker, 2011). In this study,
251 our geostationary satellite CBH retrieval algorithm aligns with the IDPS CBH
252 algorithm developed by (Baker, 2011). Utilizing the geostationary H8/AHI cloud
253 products discussed earlier, this new GEO CBH retrieval algorithm is succinctly
254 outlined below.

255 The new GEO IDPS CBH algorithm initiates the process by first retrieving the
256 cloud geometric thickness (CGT) from bottom to top. Subsequently, CGT is
257 subtracted from the corresponding cloud top height (CTH) to calculate CBH (CBH =
258 CTH – CGT). The algorithm is divided into two independent executable modules
259 based on cloud phase, distinguishing between liquid water and ice clouds. CBH of



260 water cloud retrieval requires Cloud Optical Thickness (COT or D_{COT}) and Effective
261 Radius (CER or R_{eff}) as inputs. For ice clouds, an empirical equation is employed for
262 CBH retrieval. For a more comprehensive understanding of this CBH algorithm,
263 please refer to the IDPS algorithm documentation (Baker, 2011).

264 **3.2 GEO Cloud-base height retrieval algorithm implemented in the Clouds from** 265 **Advanced Very High Resolution Radiometer Extended system**

266 As mentioned above, the accuracy of the GEO IDPS algorithm is highly
267 dependent on the initial input parameters such as cloud phase, D_{COT} and R_{eff} , which
268 may introduce some uncertainties in the final retrieval results. In contrast, a more
269 reliable statistically-based algorithm is proposed and implemented here, which is
270 named the GEO CLAVR-x (Clouds from AVHRR Extended, NOAA's operational
271 cloud processing system for the AVHRR) CBH algorithm, and it mainly refers to
272 NOAA AWG CBH algorithm (ACBA) (Noh et al., 2017; Seaman et al., 2017).

273 Similar to the GEO IDPS CBH retrieval algorithm mentioned earlier, the GEO
274 CLAVR-x CBH retrieval algorithm also initially obtains CGT and CTH, subsequently
275 calculating CBH by subtracting CGT from CTH ($CTH - CGT$). However, the specific
276 calculation method for the CGT value differs. This algorithm is suitable for both
277 single-layer and multi-layer clouds, computing CBH using the CTH at the top layer of
278 the cloud. In comparison with the former GEO IDPS CBH algorithm, the GEO
279 CLAVR-x CBH algorithm considers two additional cloud types: deep convection
280 clouds and thin cirrus clouds. For more details on this CLAVR-x CBH algorithm,
281 please refer to the original algorithm documentation (Noh et al., 2017).

282 **3.3 Random-forest-based cloud-base height estimation algorithm**

283 Random Forest (RF), one of the most significant Machine Learning (ML)
284 algorithms, was initially proposed and developed by (Breiman, 2001). It is widely
285 employed to address classification and regression problems based on the law of large
286 numbers. The RF method utilizes a forest of trees, serving as an integrated algorithm
287 that enhances overall model accuracy and generalization by combining multiple weak
288 classifiers. The final prediction is calculated through voting or averaging. The RF
289 method is well-suited for capturing complex or nonlinear relationships between
290 predictors and predictands. As mentioned earlier, this statistical or ML-based



291 algorithm has been already proven successful in retrieving CTH and CBH (Min et al.,
292 2020; Tan et al., 2020).

293 In this study, two distinct Machine Learning (ML)-based GEO CBH algorithms,
294 namely VIS+IR and IR-single (only uses observations of H8/AHI IR channels), are
295 devised to retrieve or predict the CBH using different sets of predictors. The RF
296 training of the chosen predictors is formulated as follows:

$$297 \text{CBH} = RF_{\text{reg}}[x_1, x_2, \dots, x_n], \quad (1)$$

298 where RF_{reg} denotes the regression Random Forests model, and x_i represents the i th
299 predictor. The selected predictors from H8/AHI for both the VIS+IR and IR RF
300 model training and prediction are detailed in Table 1, mainly referencing Min et al.
301 (2020) and Tan et al. (2020). The VIS+IR algorithm retrieves CBH based on NWP
302 data (atmospheric temperature and altitude profiles, total precipitable water (TPW),
303 surface temperature), surface elevation, air mass 1 (air mass $1 = 1/\cos(\text{view zenith angle})$), and air mass 2 (air mass $2 = 1/\cos(\text{solar zenith angle})$). The rationale for
304 choosing air mass and TPW is their ability to account for the potential absorption
305 effect of water vapor along the satellite viewing angle. The predictors in CBH
306 retrieval also include the IR band Brightness Temperature (BT) and VIS band
307 reflectance. The IR-single algorithm selects the same Global Forecast System (GFS)
308 NWP data as the VIS+IR algorithm but employs different view zenith angles and
309 azimuth angles.
310

311 To optimize the RF prediction model, the hyperparameters of the RF model are
312 tuned individually. The parameters and their dynamic ranges involved in tuning the
313 RF prediction models include the number of trees [100, 200, 300, 400, 500], the
314 maximum depth of trees [10, 20, 30, 40, 50], the minimum number of samples
315 required to split an internal node [2, 4, 6, 8, 10], and the minimum number of samples
316 required to be at a leaf node [1, 3, 5, 7, 9]. In this study, we set the smallest number of
317 trees in the forest to 100 and the maximum depth of the tree to 40.

318 The performance of RF models will be assessed using mean absolute error
319 (MAE), mean bias error (MBE), root mean square error (RMSE), correlation
320 coefficient (R), and standard deviation (STD) scores based on the testing dataset. In
321 the RF IR-single algorithm, 581,783 matching points are selected from H8/AHI and
322 CloudSat data for 2017. Seventy percent of these points are randomly assigned to the
323 training dataset, and the remainder serves as the testing dataset. For the RF VIS+IR
324 algorithm, a total of 418,241 matching points are chosen, with 70% randomly



325 allocated to the training set. It's important to note that the two training datasets in
326 CloudSat will also be used to verify the CBHs obtained by cloud radar and lidar. The
327 statistical formulas for evaluation are as follows:

$$328 \quad MAE = \frac{1}{n} \sum_{i=1}^n |y_i - x_i|, \quad (2)$$

$$329 \quad MBE = \frac{1}{n} \sum_{i=1}^n (y_i - x_i), \quad (3)$$

$$330 \quad RMSE = \sqrt{\frac{1}{n} \sum_{i=1}^n (y_i - x_i)^2}, \quad (4)$$

$$331 \quad R = \frac{\sum_{i=1}^n (y_i - \bar{y})(x_i - \bar{x})}{\sqrt{\sum_{i=1}^n (y_i - \bar{y})^2} \sqrt{\sum_{i=1}^n (x_i - \bar{x})^2}}, \quad (5)$$

$$332 \quad STD = \sqrt{\frac{1}{n-1} \sum_{i=1}^n (x_i - \bar{x})^2}, \quad (6)$$

333 where n is the sample number, y_i is the i th CBH retrieval result, and x_i is the i th joint
334 CloudSat/CALIOP CBH product.

335 Figure 1 displays a comparison of CBH results over the full disk at 02:00 UTC on
336 January 1, 2017, retrieved by the GEO IDPS algorithm, the GEO CLAVR-x
337 algorithm, the RF VIS+IR algorithm, and the RF IR-single algorithm. A similar
338 distribution pattern and magnitude of CBHs retrieved by these four independent
339 algorithms can be observed in Fig. 1. However, notable differences exist between
340 physics-based and ML-based algorithms. For example, the two physics-based
341 algorithms of GEO IDPS and GEO CLAVR-x yield higher CBHs. Further
342 comparisons are conducted and analyzed with spaceborne and ground-based lidar and
343 radar observations in the subsequent sections of this study.

344 4 Results and Discussions

345 4.1 Comparisons with the joint CloudSat/CALIPSO cloud-base height product

346 The H8/AHI satellite CBH data retrieved by the four algorithms are matched
347 spatially and temporally with the 2B-CLDCLASS-LIDAR cloud product from joint
348 CloudSat/CALIPSO observations in 2017. Fig. 2 presents the density scatter plot of
349 the CBHs retrieved from the GEO IDPS and GEO CLAVR-x algorithms compared
350 with the CBHs from the joint CloudSat/CALIPSO product, along with the related
351 scores of MAE, MBE, RMSE, and R calculated and labeled in each panel. The
352 calculated R exceeds the 95% significance level ($p < 0.05$). For the GEO IDPS



353 algorithm, the R is 0.62, the MAE is 1.826 km, and the MBE and RMSE are -0.232
354 and 2.642 km (Fig. 2a). In comparison, (Seaman et al., 2017) compared the
355 operational VIIRS CBH product retrieved by the similar SNPP/VIIRS IDPS algorithm
356 with the CloudSat CBH results. In their results, the R is 0.569, and the RMSE is 2.3
357 km. For the new GEO CLAVR-x algorithm (Fig. 2b), the R is 0.647, and the RMSE is
358 2.91 km. The slightly higher R and larger RMSE from two independent physics-based
359 CBH algorithms demonstrate a slightly poorer performance of these retrieval
360 algorithms for GEO satellites. Particularly, the larger RMSEs (2.642 and 2.91 km)
361 indicate weaker stabilities of the GEO IDPS and CLAVR-x CBH algorithms. In this
362 figure, more samples can be found near the 1:1 line, implying the good quality of
363 retrieved CBHs. However, in stark contrast, quite a number of CBH samples retrieved
364 by both GEO IDPS and GEO CLAVR-x algorithms (compared with the official
365 VIIRS CBH product) fall below 1.0 km, indicating relatively large errors when
366 compared with the joint CloudSat/CALIPSO CBH product. Moreover, Fig. 2 reveals
367 that relatively large errors are also found in the CBHs lower than 2 km for the four
368 independent algorithms, primarily caused by the weak penetration ability of VIS or IR
369 bands on thick and low clouds.

370 Referring to the joint CloudSat/CALIPSO CBH product, Fig. 2c and 2d present
371 the validations of the CBH results retrieved from two ML-based algorithms using the
372 VIS+IR (only retrieving the CBH during the daytime) and IR-single models. Fig. 2c
373 demonstrates the better consistency of CBH between the VIS+IR model and the joint
374 CloudSat/CALIPSO product with $R = 0.905$, $MAE = 0.817$ km, $MBE = 0.425$ km,
375 and $RMSE = 1.706$ km. Fig. 2d also displays a relatively high R of 0.876 when
376 validating the IR-single model, with $MAE = 0.882$, $MBE = -0.445$, and $RMSE =$
377 1.995 . Therefore, both VIS+IR and IR-single models can obtain high-quality CBH
378 retrieval results from geostationary imager measurements. In comparison, previous
379 studies also proposed similar ML-based algorithms for estimating CBH using FY-4A
380 satellite imager data. For example, (Tan et al., 2020) used the variables of CTH, D_{COT} ,
381 R_{eff} , cloud water path, longitude/latitude from FY-4A imager data to build the training
382 and prediction model and obtained CBH with $MAE=1.29$ km and $R=0.80$. In this
383 study, except CTH, the other Level-2 products and geolocation data
384 (longitude/latitude) used in (Tan et al., 2020) are abandoned, while the matched
385 atmospheric profile products (such as temperature and relative humidity) from NWP
386 data are added. These changes in ML-based model training and prediction lead to



387 more accurate CBH retrieval results. Note that, in accordance with the previous study
388 conducted by (Noh et al., 2017), we excluded CBH samples obtained from
389 CloudSat/CALIPSO that were smaller than 1 km in our comparisons. This exclusion
390 was primarily due to the presence of ground clutter contamination in the CloudSat
391 CPR data (Noh et al., 2017).

392 Fig. 3 displays two cross-sections of CBH from various sources overlaid with
393 CloudSat radar reflectivity (Unit = dBZ) for spatially and temporally matched cases.
394 The periods covered are from 03:16 to 04:55 UTC on January 13, 2017 (154.0°E–
395 160.0°E; 40.56°S–53.39°S) and from 05:38 to 07:17 UTC on January 14, 2017
396 (107.1°E–107.8°E; 8.35°N–11.57°N). The CloudSat radar reflectivity and joint
397 CloudSat/CALIPSO product provide insights into the vertical structure or distribution
398 of clouds and their corresponding CBHs. The results from the four GEO CBH
399 retrieval algorithms (GEO IDPS, GEO CLAVR-x, RF VIS+IR model, and RF
400 IR-single model) mentioned earlier are individually marked with different markers in
401 each panel. According to Fig. 3a, the GEO IDPS algorithm faces challenges in
402 accurately retrieving CBHs for geometrically thicker cloud samples near 157°E.
403 Optically thick mid- and upper-level cloud layers may obscure lower-level cloud
404 layers. However, the CBH results retrieved by the GEO IDPS algorithm near 155°E
405 (in Fig. 3a) and 107.4°E (in Fig. 3b) align with the joint CloudSat/CALIPSO CBH
406 product. It is worth noting that the inconsistency observed between 107.2°E and
407 107.3°E in Fig. 3b, specifically regarding the CBHs around 1 km obtained from
408 CloudSat/CALIPSO, can likely be attributed to ground clutter contamination in the
409 CloudSat CPR data (Noh et al., 2017). The GEO CLAVR-x algorithm achieves
410 improved CBH results compared to the GEO IDPS algorithm. It can even retrieve
411 CBHs for some thick cloud samples that are invalid when using the GEO IDPS
412 algorithm. However, the CBHs from the GEO CLAVR-x algorithm are noticeably
413 higher than those from the joint CloudSat/CALIPSO product. In contrast, the CBHs
414 from the two ML-based algorithms show substantially better results than those from
415 the other two physics-based algorithms. Particularly, the ML-based VIS+IR model
416 algorithm yields the best CBH results. However, compared with those from the two
417 physics-based algorithms, the CBHs from the two ML-based algorithms still exhibit a
418 significant error around 5 km.

419 Since the two RF models (VIS+IR and IR-single) select 230 typical variables to
420 fit CBHs, the important scores of these predictors in the two ML-based algorithms are



421 ranked for better optimization. In the VIS+IR model, the top-ranked predictors are
422 CTH and CTT from the H8/AHI Level-2 product (see Fig. B1 in Appendix B). It's
423 important to note that D_{COT} is a crucial and sensitive factor for these ML-based
424 algorithms. Retrieving CBH samples with relatively low D_{COT} remains challenging
425 due to the low signal-to-noise ratio when D_{COT} is low (Lin et al., 2022). To address
426 this issue, samples with D_{COT} less than 1.6 are filtered in the VIS+IR model, and
427 samples with relatively large BTs at Channel-14 are filtered in the IR-single model.
428 This filtering process significantly improves the R value from 0.869 to 0.922 in the
429 VIS+IR model and from 0.868 to 0.911 in the IR-single model. For more details on
430 the algorithm optimization, please refer to Appendix B.

431 **4.2 Comparisons with the ground-based lidar and cloud radar measurements**

432 Lidar actively emits lasers in different spectral bands into the air. When the laser
433 signal encounters cloud particles during transmission, a highly noticeable
434 backscattered signal is generated and received (Omar et al., 2009). When lidar
435 measures clouds, the intensity of the echo signal from the cloud to the laser satisfies
436 the lidar equation as follows:

$$437 \quad P(r) = C * \beta(r) * r^{-2} * \exp\left[-2 \int_0^r \sigma(z) dz\right], \quad (7)$$

438 where $P(r)$ is the intensity of the atmospheric backscattered signal received by the
439 laser telescope from the emission point in distance r (unit: Watt or W); C is the lidar
440 system instrumentation constant (unit: $\text{W} \cdot \text{km}^3 \cdot \text{sr}$); r is the detection distance (unit:
441 km); $\beta(r)$ is the backscattering coefficient at the emission point in distance r (unit:
442 $\text{km}^{-1} \cdot \text{sr}^{-1}$); $\sigma(z)$ is the extinction coefficient at the distance emission point in distance
443 z (unit: km^{-1}). This return signal is markedly distinct from atmospheric aerosol
444 scattering signals and noise, making CBH easily obtainable from the signal difference
445 or mutation (Sharma et al., 2016). In this study, continuous ground-based lidar data
446 from the Twin Astronomy Manor in Lijiang City, Yunnan Province, China (26.454°N,
447 100.0233°E, altitude = 3175 m) are used to evaluate the diurnal cycle characteristics
448 of CBHs retrieved using GEO satellite algorithms (Young and Vaughan, 2009). The
449 geographical location and photo of this station are shown in Fig. 4.

450 The ground-based lidar data at Lijiang station on December 6, 2018, and January
451 8, 2019, are selected for validation. The number of available and spatially-temporally
452 matched CBH sample points from ground-based lidar is 78 and 64 on December 6,



453 2018, and January 8, 2019, respectively. Fig 5a and 5b show the point-to-point CBH
454 comparisons between ground-based lidar and four GEO satellite CBH algorithms on
455 December 6, 2018, and January 8, 2019. It is worth noting that the retrieved CBHs of
456 the two physics-based algorithms on December 6, 2018, are in good agreement with
457 the reference values from the lidar measurements, and, in particular, the GEO
458 CLAVR-x algorithm can obtain better results. From the results on January 8, 2019,
459 more accurate diurnal cycle characteristics of CBHs are revealed by the GEO
460 CLAVR-x algorithm than by the GEO IDPS algorithm.

461 Compared with the CBHs measured by ground-based lidar, the statistics of the
462 results retrieved from the GEO IDPS algorithm are $R = 0.67$, $MAE = 3.093$ km, MBE
463 $= 0.856$ km, and $RMSE = 3.609$ km (Fig. 5c). However, for cloud samples with CBH
464 below 7.5 km, the GEO IDPS algorithm shows an obvious underestimation of CBH in
465 Fig. 5c. For the GEO CLAVR-x algorithm, it can also be seen that the matched
466 samples mostly lie near the 1:1 line with $R = 0.773$ (the optimal CBH algorithm),
467 $MAE = 1.319$ km, $MBE = 0.222$ km, and $RMSE = 1.598$ km. In addition, this figure
468 also shows the CBH comparisons between the ML-based VIS+IR model/IR-single
469 model algorithms and the lidar measurements, revealing that the retrieved CBH
470 results from the ML-based VIS+IR model are better than those from the ML-based
471 IR-single model algorithm. The comparison results between the CBHs of the
472 ML-based VIS+IR model algorithm and the lidar measurements are around the 1:1
473 line, with smaller errors and $R = 0.599$. In contrast, the R between the CBHs of the
474 ML-based IR-single model algorithm and the lidar measurements is only 0.494, with a
475 relatively large error. By comparing the retrieved CBHs with the lidar measurements
476 at Lijiang station, it indicates that CBH results from two physics-based algorithms are
477 remarkably more accurate, particularly that the GEO CLAVR-x algorithm can well
478 capture diurnal variation of CBH.

479 To further assess the accuracy and quality of the diurnal cycle of CBHs retrieved
480 with these algorithms, CBHs from another ground-based cloud radar dataset covering
481 the entire year of 2017 are also collected and used in this study. The observational
482 instrument is a Ka-band (35 GHz) Doppler millimeter-wave cloud radar (MMCR)
483 located at the Beijing Nanjiao Weather Observatory (a typical urban observation site)
484 (39.81°N , 116.47°E , altitude = 32 m; see Fig. 4), performing continuous and routine
485 observations. The MMCR provides a specific vertical resolution of 30 m and a
486 temporal resolution of 1 minute for single profile detection, based on the radar



487 reflectivity factor. In a previous study (Zhou et al., 2019), products retrieved by this
488 MMCR were utilized to investigate the diurnal variations of CTH and CBH, and
489 comparisons were made between MMCR-derived CBHs and those derived from a
490 Vaisala CL51 ceilometer. The former study also found that the average correlation
491 coefficient (R) of CBHs from different instruments reached up to 0.65. It is worth
492 noting that the basic physics principle for detecting cloud base height from both
493 spaceborne cloud profiling radar and ground-based cloud radar and lidar
494 measurements is the same. All these algorithms of detecting CBH based on the
495 manifest change of return signals between CBH and the clear sky atmosphere in the
496 vertical direction (Huo et al., 2019; Ceccaldi et al., 2013).

497 Similar to Fig. 5, Fig. 6 presents two sample groups of CBH results from the
498 cloud radar at Beijing Nanjiao station relative to the matched CBHs from the four
499 retrieval algorithms (GEO IDPS, GEO CLAVR-x, ML-based IR-single, ML-based
500 VIS+IR) on April 9–10 and July 26–28, 2017. Due to the density of points in the
501 one-year time series, the point-to-point CBH comparison results for the entire year are
502 not displayed here (monthly results are shown in the supplementary document).
503 Similar to the results at Lijiang station discussed in Fig. 5, we observe better and more
504 robust performances in retrieving diurnal cycle characteristics of CBH from the two
505 physics-based CBH retrieval algorithms. In contrast, more underestimated CBH
506 samples are retrieved by the two ML-based algorithms.

507 To further investigate the diurnal cycle characteristics of retrieved CBH from
508 GEO satellite imager measurements, Fig. 7 presents box plots of the hourly CBH
509 errors (relative to the results of cloud radar at Beijing Nanjiao station) in 2017 from
510 the four different CBH retrieval algorithms. Remarkably, there are significant
511 underestimations of the CBHs retrieved from the two ML-based algorithms. The
512 ML-based VIS+IR method achieves relatively better results than the ML-based
513 IR-single method during the daytime. Comparing the two ML-based algorithms, the
514 errors of the IR-single model algorithm have a similar standard deviation (2.80 km) to
515 those of the VIS+IR model algorithm (2.69 km) during the daytime. For the IR-single
516 model algorithm, it can be applied during both daytime and nighttime, its nighttime
517 performance degrades slightly, with an averaged RMSE (3.88 km) higher than that of
518 daytime (3.56 km). To the best of our knowledge, there is no alternative nighttime
519 CBH product for geostationary satellite imagers right now. The nighttime CBH of the
520 IR-single model algorithm is the only choice that should be used with discretion.



521 Fig. 8a displays scatter plots and relevant statistics of the CBHs retrieved from
522 the GEO IDPS algorithm against the CBHs from cloud radar. The CBHs from the
523 GEO IDPS algorithm align well with the matched CBHs from cloud radar at Beijing
524 Nanjiao station, with $R = 0.515$, $MAE = 2.078$ km, $MBE = 1.168$ km, and $RMSE =$
525 2.669 km. In Fig. 8b, the GEO CLAVR-x algorithm shows better results with $R =$
526 0.573 , $MAE = 2.059$ km, $MBE = -0.204$ km, and $RMSE = 2.601$ km. It not surprised
527 that Figs. 8c and 8d reveal obvious underestimated CBH results from the two
528 ML-based CBH algorithms. Particularly, the CBH results from the ML-based VIS+IR
529 model algorithm concentrate in the range of 2.5 km to 5 km. Therefore, Fig. 5 to Fig.
530 8 further substantiates the weak diurnal variations captured by ML-based techniques,
531 primarily attributed to the scarcity of comprehensive CBH training samples
532 throughout the entire day. Besides, although the two robust physics-based algorithms
533 of GEO IDPS and GEO CLAVR-x (the optimal one) can retrieve high-quality CBHs
534 from H8/AHI data, especially the diurnal cycle of CBH during the daytime, they still
535 struggle to retrieve CBHs below 1 km.

536 5. Conclusions and discussion

537 To explore and argue the optimal and most robust CBH retrieval algorithm from
538 geostationary satellite imager measurements, particularly focusing on capturing the
539 typical diurnal cycle characteristics of CBH, this study employs four different
540 retrieval algorithms (two physics-based and two ML-based algorithms). High
541 spatial-temporal resolution CBHs are retrieved using the H8/AHI data from 2017 and
542 2018. To assess the accuracies of the retrieved CBHs, point-to-point validations are
543 conducted based on spatially-temporally matched CBHs from the joint
544 CloudSat/CALIOP product, as well as ground-based lidar and cloud radar
545 observations in China. The main findings and conclusions are outlined below.

546 Four independent CBH retrieval algorithms, namely physics-based GEO IDPS,
547 GEO CLAVR-x, ML-based VIS+IR, and ML-based IR-single, have been developed
548 and utilized to retrieve CBHs from GEO H8/AHI data. The two physics-based
549 algorithms utilize cloud top and optical property products from AHI as input
550 parameters to retrieve high spatial-temporal resolution CBHs, with operations limited
551 to daytime. In contrast, the ML-based VIS+IR model and IR-single model algorithms
552 use the matched joint CloudSat/CALIOP CBH product as true values for building RF



553 prediction models. Notably, the ML-based IR-single algorithm, which relies solely on
554 infrared band measurements, can retrieve CBH throughout the day.

555 The accuracy of CBHs retrieved from the four independent algorithms is verified
556 using the joint CloudSat/CALIOP CBH products for the year 2017. The GEO IDPS
557 algorithm shows an R of 0.62 and an RMSE of 2.642 km. The GEO CLAVR-x
558 algorithm provides more accurate CBHs with an R of 0.647 and RMSE of 2.91 km.
559 After filtering samples with optical thickness less than 1.6 and brightness temperature
560 (at 11 μm band) greater than 281 K, the ML-based VIS+IR and ML-based IR-single
561 algorithms achieve higher accuracy with an R(RMSE) of 0.922(1.214 km) and
562 0.911(1.415 km), respectively. This indicates strong agreement between the two
563 ML-based CBH algorithms and the CloudSat/CALIOP CBH product.

564 However, in stark contrast, the results from the physics-based algorithms are
565 superior to those from the ML-based algorithms (with R and RMSE of 0.592/2.86 km
566 and 0.385/3.88 km, respectively) when compared with ground-based CBH
567 observations such as lidar and cloud radar. In the comparison with the cloud radar at
568 Beijing Nanjiao station in 2017, the R of the GEO CLAVR-x algorithm is 0.573,
569 while the R of the GEO IDPS algorithm is 0.515. Meanwhile, notable differences are
570 observed in the CBHs from both ML-based algorithms. Similar conclusions are also
571 evident in the 2-day comparisons at Yunnan Lijiang station.

572 The near-perfect CBH results from the two ML-based algorithms ($R > 0.91$) can
573 likely be attributed to the use of the same training and validation dataset source as the
574 joint CloudSat/CALIOP product. However, this dataset has limited spatial coverage
575 and small temporal variation, potentially limiting the representativeness of the
576 training data. In contrast, the GEO CLAVR-x algorithm demonstrates the best
577 performance and highest accuracy in retrieving CBH from geostationary satellite data.
578 Notably, its results align well with those from ground-based lidar and cloud radar
579 during the daytime. However, both physics-based methods, utilizing CloudSat CPR
580 data for regression, struggle to accurately retrieve CBHs below 1 km, as the lowest 1
581 km above ground level of this data is affected by ground clutter.

582 Additionally, despite utilizing the same physics principles in spaceborne and
583 ground-based lidar/radar CBH algorithms, the previous study (Thorsen et al., 2011)
584 has highlighted differences in profiles between them. Therefore, this factor could
585 contribute to the relatively poorer results in CBH retrieval by ML-based algorithms
586 compared to ground-based lidar and radar. The analysis and discussion above suggest



587 that machine learning (ML)-based algorithms are constrained by the size of their
588 datasets. Therefore, in scenarios involving a large time scope, such as climate
589 research, it is more reasonable to opt for physics-based cloud base height algorithms.

590 Note that the ML-based algorithms still demonstrate better CBH retrievals using
591 the spaceborne joint CloudSat/CALIOP detection method. Ideally, if more spaceborne
592 cloud profiling radars with different passing times (covering all day) can be included
593 in the training dataset, the promising ML technique will certainly generate a higher
594 quality CBH product with more comprehensive observations. The CBH product using
595 ML-based algorithms should continue to be improved in future work.

596

597

598

599 *Data availability.* The authors would like to acknowledge NASA, JMA, University of
600 Colorado, and NOAA for freely providing the MODIS
601 (<https://ladsweb.modaps.eosdis.nasa.gov/search>), CloudSat/CALIOP
602 (<https://www.cloudsat.cira.colostate.edu/>), Himawari-8 (<ftp.ptree.jaxa.jp>), and GFS
603 NWP (<ftp://nomads.ncdc.noaa.gov/GFS/Grid4>) data online, respectively.

604

605

606 *Author contributions.* MM proposed the essential research idea. MW, MM, JL, HL,
607 BC, and YL performed the analysis and drafted the manuscript. ZY and NX provided
608 useful comments. All the authors contributed to the interpretation and discussion of
609 results and the revision of the manuscript.

610

611

612 *Competing interests.* The authors declare that they have no conflict of interest.

613

614

615 *Acknowledgements.* The authors would like to acknowledge NASA, JMA, University
616 of Colorado, and NOAA for freely providing satellite data online, respectively. The
617 authors thank NOAA, NASA, and their VIIRS algorithm working groups (AWG) for
618 freely providing the VIIRS cloud base height algorithm theoretical basic



619 documentations (ATBD). In addition, the authors appreciate the power computer tools
620 developed by the Python and scikit-learn groups (<http://scikit-learn.org>). Besides the
621 authors also thank Rundong Zhou and Pan Xia for drawing some pictures of this
622 manuscript. Last but not the least, the authors sincerely thank Prof. Yong Zhang and
623 Prof. Jianping Guo for freely providing cloud base height results retrieved by
624 ground-based cloud radar at Beijing Nanjiao station. This work was supported partly
625 by the Guangdong Major Project of Basic and Applied Basic Research (Grant
626 2020B0301030004), National Natural Science Foundation of China under Grants
627 42175086 and U2142201, FengYun Meteorological Satellite Innovation Foundation
628 under Grant FY-APP-ZX-2022.0207, and Innovation Group Project of Southern
629 Marine Science and Engineering Guangdong Laboratory (Zhuhai) (No. 311022006).
630 We would like to thank the editor and anonymous reviewers for their thoughtful
631 suggestions and comments.

632

633

634 **Appendix A**

635 Based on the previously discussed description of two physics-based cloud base
636 height (CBH) retrieval algorithms (GEO IDPS and GEO CLAVR-x retrieval
637 algorithms), cloud products such as cloud top height (CTH), effective particle radius
638 (R_{eff}), and cloud optical thickness (D_{COT}) will be utilized in both algorithms. To
639 validate the reliability of these cloud products derived from the Advanced Himawari
640 Imager (AHI) aboard the Himawari-8 (H8), a pixel-by-pixel comparison is conducted
641 with analogous MODIS Collection-6.1 Level-2 cloud products. Both Aqua and Terra
642 MODIS Level-2 cloud products (MOD06 and MYD06) are accessible for free
643 download from the MODIS official website. For verification purposes, the
644 corresponding Level-2 cloud products from January, April, July, and October of 2018
645 are chosen to assess CTH, D_{COT} , and R_{eff} retrieved by H8/AHI.

646 Fig. S2 (in the supplementary document) shows the spatially-temporally matched
647 case comparisons of CTH, D_{COT} and R_{eff} from H8/AHI and Terra/MODIS (MYD06)
648 at 03:30 UTC on January 15, 2018. It can be seen that the CTH, D_{COT} and R_{eff} from
649 H8/AHI are in good agreement with the matched MODIS cloud products. However,
650 there are still some differences in R_{eff} at the regions near 35°N, 110°E in Figs. S2d



651 and S2c. The underestimated R_{eff} values from H8/AHI relative to MODIS have been
652 reported in previous studies. (Letu et al., 2019) compared the ice cloud products
653 retrieved from AHI and MODIS, and concluded that the R_{eff} from both products differ
654 remarkably in the ice cloud region and the D_{COT} from them are roughly similar.
655 However, the D_{COT} from AHI data is higher in some areas. Looking again at the cloud
656 optical thickness that at the same time, the slight underestimation of H8/AHI D_{COT}
657 can be found in Figs. S2e and S2f. Fig. S3 (in the supplementary document) shows
658 another case at 02:10 UTC on January 15, 2018. Despite of the good consistence
659 between H8/AHI and MODIS cloud products, there are slight differences in CTH in
660 the area around 40°S–40.5°S, 100°E–110°E in Figs. S3a and S3b. Besides, as shown
661 in Fig. S2, there are still underestimations in the R_{eff} of H8/AHI.

662 To further compare and validate these three H8/AHI cloud products, the
663 spatially-temporally matched samples from H8/AHI and Aqua/Terra MODIS in four
664 months of 2018 are counted within the three intervals of 0.1 km (CTH), 1.0 μm (R_{eff}),
665 and 1 (D_{COT}) in Fig. S4 (in the supplementary document). The corresponding mean
666 absolute error, mean bias error, root mean square error and correlation coefficient (R)
667 values are also calculated and marked in each subfigure. As can be seen, the R of
668 CTH is around 0.75 in all four months and is close to 0.8 in August. The results of
669 D_{COT} show the highest R , reaching above 0.8. In contrast, the underestimation trend in
670 R_{eff} is also shown in this figure. These different consistencies between two
671 satellite-retrieved cloud products may be attributed to: (1) different spatial-temporal
672 resolutions between H8/AHI and MODIS; (2) different wavelength bands, bulk
673 scattering model, and specific algorithm used for retrieving cloud products; (3)
674 different view zenith angle between GEO and low-earth-orbit satellite platforms (Letu
675 et al., 2019). In addition, other external factors such as surface type also can affect the
676 retrieval of cloud product. However, according to Fig. S4, the bulk of the analyzed
677 samples are still around the 1:1 line, indicating the good quality of H8/AHI cloud
678 products.

679

680 **Appendix B**

681 The ML-based visible (VIS)+infrared (IR) model algorithm mentioned above
682 uses 230 typical variables (see Table 1) as model predictors, and the importance
683 scores of top-30 predictors are ranked in Fig. S5 (in the supplementary document). It
684 can be seen that the most important variables are CTH and cloud top temperature, and



685 D_{COT} is an important or sensitive factor affecting these two quantities. A sensitivity
686 test is also performed to further investigate the potential influence of D_{COT} on the
687 CBH retrieval by the VIS+IR model (see Table S1 in the supplementary document).
688 From Fig. S7a, we find that the samples with D_{COT} lower than 5 cause the relatively
689 large CBH errors compared with the matched CBHs from the joint CALIPSO
690 (Cloud-Aerosol Lidar and Infrared Pathfinder Satellite Observation)/CloudSat
691 product.

692 According to the results in this Fig. S7b, we may filter the samples with
693 relatively small D_{COT} to further improve the accuracy of CBH retrieval by the VIS+IR
694 model (see Table S1). Fig. B3b shows that after filtering the samples with the D_{COT}
695 less than 1.6, the R increases from 0.895 to 0.922, implying a better performance of
696 CBH retrieval. According to the ranking of predictor importance (see Fig. S6 in the
697 supplementary document), we also conduct another sensitivity test on the BT
698 observed by H8/AHI IR Channel-14 (Cha14) at 11 μm , which plays an important role
699 in the IR-single model. Fig. S7c shows that the BT values of H8/AHI Channel-14
700 ranges from 160 K to 316 K, and the samples with BT higher than 300 K show large
701 CBH errors. Similarly, by filtering the samples with BT higher than 281 K, we can get
702 a better IR-single model algorithm for retrieving high-quality CBH (see Table S2 in
703 the supplementary document). Fig. S7d also proves that the R value increases from
704 0.868 to 0.911.

705

706

707 Reference

- 708 Aydin, K. and Singh, J.: Cloud Ice Crystal Classification Using a 95-GHz
709 Polarimetric Radar, *Journal of Atmospheric and Oceanic Technology*, 21,
710 1679–1688, <https://doi.org/10.1175/JTECH1671.1>, 2004.
- 711 Baker, N.: Joint Polar Satellite System (JPSS) VIIRS Cloud Base Height Algorithm
712 Theoretical Basis Document (ATBD), 2011.
- 713 Baum, B., Menzel, W. P., Frey, R., Tobin, D., Holz, R., and Ackerman, S.: MODIS
714 cloud top property refinements for Collection 6, *Journal of Applied
715 Meteorology and Climatology*, 51, 1145-1163, 10.1175/JAMC-D-11-0203.1,



- 716 2012.
- 717 Bessho, K., Date, K., Hayashi, M., Ikeda, A., Imai, T., Inoue, H., Kumagai, Y.,
718 Miyakawa, T., Murata, H., Ohno, T., Okuyama, A., Oyama, R., Sasaki, Y.,
719 Shimazu, Y., Shimoji, K., Sumida, Y., Suzuki, M., Taniguchi, H., Tsuchiyama,
720 H., Uesawa, D., Yokota, H., and Yoshida, R.: An introduction to
721 Himawari-8/9—Japan's new-generation geostationary meteorological satellites,
722 Journal of the Meteorological Society of Japan, 94, 151-183,
723 10.2151/jmsj.2016-009, 2016.
- 724 Breiman, L.: Random forests, Machine Learning, 45, 5-32, 2001.
- 725 Ceccaldi, M., Delanoë, J., Hogan, R. J., Pounder, N. L., Protat, A., and Pelon, J.: From
726 CloudSat-CALIPSO to EarthCare: Evolution of the DARDAR cloud
727 classification and its comparison to airborne radar-lidar observations, Journal
728 of Geophysical Research: Atmospheres, 118, 7962-7981, 10.1002/jgrd.50579,
729 2013.
- 730 Forsythe, J. M., Haar, T. H. V., and Reinke, D. L.: Cloud-Base height estimates using
731 a combination of Meteorological Satellite Imagery and Surface Reports,
732 Journal of Applied Meteorology and Climatology, 39, 2336–2347,
733 [https://doi.org/10.1175/1520-0450\(2000\)039<2336:CBHEUA>2.0.CO;2](https://doi.org/10.1175/1520-0450(2000)039<2336:CBHEUA>2.0.CO;2),
734 2000.
- 735 Håkansson, N., Adok, C., Thoss, A., Scheirer, R., and Hörnquist, S.: Neural network
736 cloud top pressure and height for MODIS, Atmospheric Measurement
737 Techniques, 11, 3177–3196, 10.5194/amt-11-3177-2018, 2018.
- 738 Hansen, B.: A Fuzzy Logic–Based Analog Forecasting System for Ceiling and
739 Visibility, Weather and Forecasting, 22, 1319-1330,
740 10.1175/2007waf2006017.1, 2007.
- 741 Hartmann, D. L. and Larson, K.: An important constraint on tropical cloud - climate
742 feedback, Geophys Res Lett, 29, 12-11-12-14, 10.1029/2002gl015835, 2002.
- 743 Heidinger, A. and Pavolonis, M.: Gazing at cirrus clouds for 25 years through a split
744 window, part 1: Methodology, Journal of Applied Meteorology and
745 Climatology, 48, 1110-1116, 10.1175/2008JAMC1882.1, 2009.



- 746 Heidinger, A. K., Bearson, N., Foster, M. J., Li, Y., Wanzong, S., Ackerman, S., Holz,
747 R. E., Platnick, S., and Meyer, K.: Using sounder data to improve cirrus cloud
748 height estimation from satellite imagers, *Journal of Atmospheric and Oceanic*
749 *Technology*, 36, 1331-1342, 10.1175/jtech-d-18-0079.1, 2019.
- 750 Heymsfield, A. J., Bansemer, A., Matrosov, S., and Tian, L.: The 94-GHz radar dim
751 band: Relevance to ice cloud properties and CloudSat, *Geophys. Res. Lett.*, 35,
752 10.1029/2007GL031361, 2008.
- 753 Hirsch, E., Agassi, E., and Koren, I.: A novel technique for extracting clouds base
754 height using ground based imaging, *Atmospheric Measurement Techniques*, 4,
755 117-130, 10.5194/amt-4-117-2011, 2011.
- 756 Hunt, W. H., Winker, D. M., Vaughan, M. A., Powell, K. A., Lucker, P. L., and
757 Weimer, C.: CALIPSO lidar description and performance assessment, *J.*
758 *Atmos. Oceanic. Technol.*, 26, 2009.
- 759 Huo, J., Bi, Y., Lü, D., and Duan, S.: Cloud Classification and Distribution of Cloud
760 Types in Beijing Using Ka-Band Radar Data, *Advances in Atmospheric*
761 *Sciences*, 36, 793-803, 10.1007/s00376-019-8272-1, 2019.
- 762 Hutchison, K., Wong, E., and Ou, S. C.: Cloud base heights retrieved during night-
763 time conditions with MODIS data, *Int J Remote Sens*, 27, 2847-2862,
764 10.1080/01431160500296800, 2006.
- 765 Hutchison, K. D.: The retrieval of cloud base heights from MODIS and
766 three-dimensional cloud fields from NASA's EOS Aqua mission, *Int J Remote*
767 *Sens*, 23, 5249-5265, 10.1080/01431160110117391, 2002.
- 768 Iwabuchi, H., Putri, N. S., Saito, M., Tokoro, Y., Sekiguchi, M., Yang, P., and Baum,
769 B. A.: Cloud Property Retrieval from Multiband Infrared Measurements by
770 Himawari-8, *Journal of the Meteorological Society of Japan. Ser. II*, 96B,
771 27-42, 10.2151/jmsj.2018-001, 2018.
- 772 Kalnay, E., Kanamitsu, M., Kistler, R., Collins, W., Deaven, D., Gandin, L., Iredell,
773 M., Saha, S., White, G., Woollen, J., Zhu, Y., Leetmaa, A., Reynolds, R.,
774 Chelliah, M., Ebisuzaki, W., W.Higgins, Janowiak, J., Mo, K. C., Ropelewski,
775 C., and Wang, J.: The NCEP NCAR 40-Year Reanalysis Project, 1996.



- 776 Kühnlein, M., Appelhans, T., Thies, B., and Nauß, T.: Precipitation Estimates from
777 MSG SEVIRI Daytime, Nighttime, and Twilight Data with Random Forests,
778 Journal of Applied Meteorology and Climatology, 53, 2457-2480,
779 10.1175/jamc-d-14-0082.1, 2014.
- 780 Letu, H., Nagao, T. M., Nakajima, T. Y., Riedi, J., Ishimoto, H., Baran, A. J., Shang,
781 H., Sekiguchi, M., and Kikuchi, M.: Ice cloud properties from
782 Himawari-8/AHI next-generation geostationary satellite: Capability of the
783 AHI to monitor the DC cloud generation process, IEEE Transactions on
784 Geoscience and Remote Sensing, 57, 3229-3239, 10.1109/tgrs.2018.2882803,
785 2019.
- 786 Li, Y., Yi, B., and Min, M.: Diurnal variations of cloud optical properties during
787 day-time over China based on Himawari-8 satellite retrievals, Atmospheric
788 Environment, 277, 119065, 10.1016/j.atmosenv.2022.119065, 2022.
- 789 Liang, Y., Min, M., Yu, Y., Wang, X., and Xia, P.: Assessing diurnal cycle of cloud
790 covers of Fengyun-4A geostationary satellite based on the manual observation
791 data in China, IEEE Transactions on Geoscience and Remote Sensing, 61,
792 10.1109/TGRS.2023.3256365, 2023.
- 793 Lin, H., Li, Z., Li, J., Zhang, F., Min, M., and Menzel, W. P.: Estimate of daytime
794 single-layer cloud base height from Advanced Baseline Imager measurements,
795 Remote Sensing of Environment, 274, 112970, 10.1016/j.rse.2022.112970,
796 2022.
- 797 Lu, X., Mao, F., Rosenfeld, D., Zhu, Y., Pan, Z., and Gong, W.: Satellite retrieval of
798 cloud base height and geometric thickness of low-level cloud based on
799 CALIPSO, Atmospheric Chemistry and Physics, 21,
800 10.5194/acp-21-11979-2021, 2021.
- 801 Meerkötter, R. and Bugliaro, L.: Diurnal evolution of cloud base heights in convective
802 cloud fields from MSG/SEVIRI data Atmospheric Chemistry and Physics, 9,
803 1767–1778, 10.5194/acp-9-1767-2009, 2009.
- 804 Miller, R. M., Rauber, R. M., Girolamo, L. D., Rilloraza, M., Fu, D., McFarquhar, G.
805 M., Nesbitt, S. W., Ziemba, L. D., Woods, S., and Thornhill, K. L.: Influence



- 806 of natural and anthropogenic aerosols on cloud base droplet size distributions
807 in clouds over the South China Sea and West Pacific, *Atmospheric Chemistry*
808 and *Physics*, 23, 8959–8977, 10.5194/acp-23-8959-2023, 2023.
- 809 Miller, S. D., Rogers, M. A., Haynes, J. M., Sengupta, M., and Heidinger, A. K.:
810 Short-term solar irradiance forecasting via satellite/model coupling, *Solar*
811 *Energy*, 168, 102-117, 10.1016/j.solener.2017.11.049, 2018.
- 812 Min, M. and Zhang, Z.: On the influence of cloud fraction diurnal cycle and sub-grid
813 cloud optical thickness variability on all-sky direct aerosol radiative forcing,
814 *Journal of Quantitative Spectroscopy and Radiative Transfer*, 142, 25-36,
815 10.1016/j.jqsrt.2014.03.014., 2014.
- 816 Min, M., Li, J., Wang, F., Liu, Z., and Menzel, W. P.: Retrieval of cloud top properties
817 from advanced geostationary satellite imager measurements based on machine
818 learning algorithms, *Remote Sensing of Environment*, 239, 111616,
819 10.1016/j.rse.2019.111616 2020.
- 820 Min, M., Chen, B., Xu, N., He, X., Wei, X., and Wang, M.: Nonnegligible diurnal and
821 long-term variation characteristics of the calibration biases in
822 Fengyun-4A/AGRI infrared channels based on the oceanic drifter data, *IEEE*
823 *Transactions on Geoscience and Remote Sensing*, 60, 1-15,
824 10.1109/TGRS.2022.3160450, 2022.
- 825 Min, M., Wu, C., Li, C., Liu, H., Xu, N., Wu, X., Chen, L., Wang, F., Sun, F., Qin, D.,
826 Wang, X., Li, B., Zheng, Z., Cao, G., and Dong, L.: Developing the science
827 product algorithm testbed for Chinese next-generation geostationary
828 meteorological satellites: FengYun-4 series, *Journal of Meteorological*
829 *Research*, 31, 708-719, 10.1007/s13351-017-6161-z, 2017.
- 830 Noh, Y.-J., Forsythe, J. M., Miller, S. D., Seaman, C. J., Li, Y., Heidinger, A. K.,
831 Lindsey, D. T., Rogers, M. A., and Partain, P. T.: Cloud-base height estimation
832 from VIIRS. Part II: A statistical algorithm based on A-Train satellite data,
833 *Journal of Atmospheric and Oceanic Technology*, 34, 585–598,
834 10.1175/JTECH-D-16-0110.1, 2017.
- 835 Omar, A., Winker, D., Kittaka, C., Vaughan, M., Liu, Z., Hu, Y., Trepte, C., Rogers, R.,



- 836 Ferrare, R., Kuehn, R., and Hostetler, C.: The CALIPSO automated aerosol
837 classification and lidar ratio selection algorithm, *J. Atmos. Oceanic. Technol.*,
838 26, 1994-2014, 10.1175/2009JTECHA1231, 2009.
- 839 Platnick, S., Meyer, K. G., King, M. D., Wind, G., Amarasinghe, N., Marchant, B.,
840 Arnold, G. T., Zhang, Z., Hubanks, P. A., Holz, R. E., Yang, P., Ridgway, W. L.,
841 and Riedi, J.: The MODIS cloud optical and microphysical products:
842 Collection 6 updates and examples from Terra and Aqua, *IEEE Trans Geosci*
843 *Remote Sens*, 55, 502-525, 10.1109/TGRS.2016.2610522, 2017.
- 844 Rosenfeld, D., Zheng, Y., Hashimshoni, E., Pohlker, M. L., Jefferson, A., Pohlker, C.,
845 Yu, X., Zhu, Y., Liu, G., Yue, Z., Fischman, B., Li, Z., Giguzin, D., Goren, T.,
846 Artaxo, P., Barbosa, H. M., Poschl, U., and Andreae, M. O.: Satellite retrieval
847 of cloud condensation nuclei concentrations by using clouds as CCN chambers,
848 *Proc. Natl. Acad. Sci.*, 113, 5828-5834, 10.1073/pnas.1514044113, 2016.
- 849 Sassen, K. and Wang, Z.: Classifying clouds around the globe with the CloudSat radar:
850 1-year of results, *Geophys. Res. Lett.*, 35, 1-5, doi:10.1029/2007GL032591,
851 2008.
- 852 Seaman, C. J., Noh, Y.-J., Miller, S. D., Heidinger, A. K., and Lindsey, D. T.:
853 Cloud-base height estimation from VIIRS. Part I: Operational algorithm
854 validation against CloudSat, *Journal of Atmospheric and Oceanic Technology*,
855 34, 567-583, 10.1175/jtech-d-16-0109.1, 2017.
- 856 Sharma, S., Vaishnav, R., Shukla, M. V., Kumar, P., Kumar, P., Thapliyal, P. K., Lal, S.,
857 and Acharya, Y. B.: Evaluation of cloud base height measurements from
858 Ceilometer CL31 and MODIS satellite over Ahmedabad, India, *Atmospheric*
859 *Measurement Techniques*, 9, 711-719, 10.5194/amt-9-711-2016, 2016.
- 860 Stubenrauch, C. J., Rossow, W. B., Kinne, S., Ackerman, S., Cesana, G., Chepfer, H.,
861 Di Girolamo, L., Getzewich, B., Guignard, A., Heidinger, A., Maddux, B. C.,
862 Menzel, W. P., Minnis, P., Pearl, C., Platnick, S., Poulsen, C., Riedi, J.,
863 Sun-Mack, S., Walther, A., Winker, D., Zeng, S., and Zhao, G.: Assessment of
864 global cloud datasets from satellites: project and database initiated by the
865 GEWEX radiation panel, *Bulletin of the American Meteorological Society*, 94,



- 866 1031-1049, 10.1175/bams-d-12-00117.1, 2013.
- 867 Su, T., Zheng, Y., and Li, Z.: Methodology to determine the coupling of continental
868 clouds with surface and boundary layer height under cloudy conditions from
869 lidar and meteorological data, *Atmospheric Chemistry and Physics*, 22,
870 1453-1466, 10.5194/acp-22-1453-2022, 2022.
- 871 Tan, Z., Huo, J., Ma, S., Han, D., Wang, X., Hu, S., and Yan, W.: Estimating cloud
872 base height from Himawari-8 based on a random forest algorithm, *Int J*
873 *Remote Sens*, 42, 2485-2501, 10.1080/01431161.2020.1854891, 2020.
- 874 Tana, G., Ri, X., Shi, C., Ma, R., Letu, H., Xu, J., and Shi, J.: Retrieval of cloud
875 microphysical properties from Himawari-8/AHI infrared channels and its
876 application in surface shortwave downward radiation estimation in the sun
877 glint region, *Remote Sensing of Environment*, 29, 113548,
878 10.1016/j.rse.2023.113548, 2023.
- 879 Thorsen, T. J., Fu, Q., and Comstock, J.: Comparison of the CALIPSO satellite and
880 ground-based observations of cirrus clouds at the ARM TWP sites, *Journal of*
881 *Geophysical Research: Atmospheres*, 116, 10.1029/2011jd015970, 2011.
- 882 Viúdez-Mora, A., Costa-Surós, M., Calbó, J., and González, J. A.: Modeling
883 atmospheric longwave radiation at the surface during overcast skies: The role
884 of cloud base height, *Journal of Geophysical Research: Atmospheres*, 120,
885 199-214, 10.1002/2014jd022310, 2015.
- 886 Wang, F., Min, M., Xu, N., Liu, C., Wang, Z., and Zhu, L.: Effects of linear
887 calibration errors at low temperature end of thermal infrared band: Lesson
888 from failures in cloud top property retrieval of FengYun-4A geostationary
889 satellite, *IEEE Transactions on Geoscience and Remote Sensing*, 60, 5001511,
890 10.1109/TGRS.2022.3140348, 2022.
- 891 Wang, T., Shi, J., Ma, Y., Letu, H., and Li, X.: All-sky longwave downward radiation
892 from satellite measurements: General parameterizations based on LST, column
893 water vapor and cloud top temperature, *ISPRS Journal of Photogrammetry and*
894 *Remote Sensing*, 161, 52-60, 10.1016/j.isprs.2020.01.011, 2020.
- 895 Wang, X., Min, M., Wang, F., Guo, J., Li, B., and Tang, S.: Intercomparisons of cloud



- 896 mask product among Fengyun-4A, Himawari-8 and MODIS, IEEE
897 Transactions on Geoscience and Remote Sensing, 57, 8827-8839,
898 10.1109/TGRS.2019.2923247 2019.
- 899 Wang, Z., Vane, D., Stephens, G., Reinke, D., and TBD: Level 2 combined radar and
900 lidar cloud scenario classification product process description and interface
901 control document, 2012.
- 902 Warren, S. G. and Eastman, R.: Diurnal Cycles of Cumulus, Cumulonimbus, Stratus,
903 Stratocumulus, and Fog from Surface Observations over Land and Ocean, J
904 Climate, 27, 2386-2404, 10.1175/jcli-d-13-00352.1, 2014.
- 905 Yang, J., Li, S., Gong, W., Min, Q., Mao, F., and Pan, Z.: A fast cloud geometrical
906 thickness retrieval algorithm for single-layer marine liquid clouds using
907 OCO-2 oxygen A-band measurements, Remote Sensing of Environment, 256,
908 10.1016/j.rse.2021.112305, 2021.
- 909 Young, S. A. and Vaughan, M. A.: The retrieval of profiles of particulate extinction
910 from Cloud Aerosol Lidar Infrared Pathfinder Satellite Observations
911 (CALIPSO) data: Algorithm description, J. Atmos. Oceanic. Technol., 26,
912 1105-1119, 10.1175/2008JTECHA1221.1, 2009.
- 913 Zhang, Y., Zhang, L., Guo, J., Feng, J., Cao, L., Wang, Y., Zhou, Q., Li, L., Li, B., Xu,
914 H., Liu, L., An, N., and Liu, H.: Climatology of cloud-base height from
915 long-term radiosonde measurements in China, Advances in Atmospheric
916 Sciences, 35, 158-168, 10.1007/s00376-017-7096-0, 2018.
- 917 Zheng, Y., Sakradzija, M., Lee, S.-S., and Li, Z.: Theoretical Understanding of the
918 Linear Relationship between Convective Updrafts and Cloud-Base Height for
919 Shallow Cumulus Clouds. Part II: Continental Conditions, J Atmos Sci, 77,
920 1313-1328, 10.1175/jas-d-19-0301.1, 2020.
- 921 Zhou, Q., Zhang, Y., Li, B., Li, L., Feng, J., Jia, S., Lv, S., Tao, F., and Guo, J.:
922 Cloud-base and cloud-top heights determined from a ground-based cloud radar
923 in Beijing, China, Atmospheric Environment, 201, 381-390,
924 10.1016/j.atmosenv.2019.01.012, 2019.
- 925 Zhou, R., Pan, X., Xiaohu, Z., Na, X., and Min, M.: Research progress and prospects



926 of atmospheric motion vector based on meteorological satellite images,
927 Reviews of Geophysics and Planetary Physics (In Chinese), 55, 184-194,
928 10.19975/j.dqyxx.2022-077, 2024.

929 Zhu, Y., Rosenfeld, D., Yu, X., Liu, G., Dai, J., and Xu, X.: Satellite retrieval of
930 convective cloud base temperature based on the NPP/VIIRS Imager, Geophys
931 Res Lett, 41, 1308-1313, 10.1002/2013gl058970, 2014.

932

933

934

935

936

937

938

939

940

941

942

943

944

945

946

947

948

949

950

951

952

953

954

955

956

957



958

959

960

961

962

Tables and Figures

963

964 **Table 1.** Predictand and predictor variables for both visible (VIS)+infrared (IR) model

965 and IR-single regression model training, which are divided according to the different

966 predictor variables from satellite and NWP data

Predictand	Cloud base height from the joint CloudSat/CALIPSO product	
Predictor [satellite measurements]	IR-single	BT(3.9 μ m), BT(6.2 μ m), BT(6.9 μ m), BT(7.3 μ m), BT(8.6 μ m), BT(9.6 μ m), BT(10.4 μ m), BT(11.2 μ m), BT(12.4 μ m), BT(13.3 μ m), BTD(11.2–12.4 μ m), BTD(11.2–13.3 μ m) [Unit = K], Air Mass (1/cos(VZA)), View azimuth angles [Unit = degree], Cloud top height from H8/AHI [unit: m], Cloud top temperature from H8/AHI [unit: K]
	VIS+IR	Ref(0.47 μ m), Ref(0.51 μ m), Ref(0.64 μ m), Ref(0.86 μ m), Ref(1.64 μ m), Ref(2.25 μ m), BT(3.9 μ m), BT(6.2 μ m), BT(6.9 μ m), BT(7.3 μ m), BT(8.6 μ m), BT(9.6 μ m), BT(10.4 μ m), BT(11.2 μ m), BT(12.4 μ m), BT(13.3 μ m), BTD(11.2–12.4 μ m), BTD(11.2–13.3 μ m) [Unit = K], Air Mass(1/cos(VZA)), Air Mass(1/cos(SZA)), View/Solar Azimuth angles [Unit = degree], Cloud top height from H8/AHI [unit: m], Cloud top temperature from H8/AHI [unit: K]
Predictor [GFS NWP]	IR-single/	Altitude profile (from surface to about 21 km, 67 layers) [unit: m], Temperature profile (from surface to about 21 km, 67 layers) [unit: K],
	VIS+IR	Relative humidity profile (from surface to about 21 km, 67 layers) [unit: %], Total precipitable water, Surface temperature [unit: K]
Predictor [other]	IR-single/ VIS+IR	Surface elevation [unit: m]

967 Notes: VZA = view zenith angle [unit: degree]; SZA = solar zenith angle [unit:

968 degree]

969

970

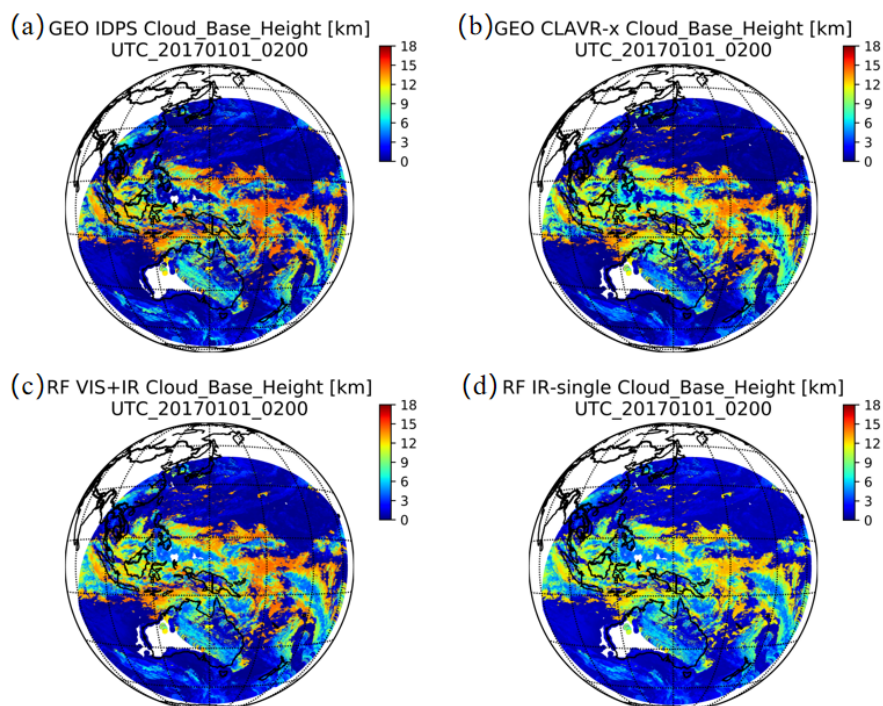
971

972

973



974
975
976
977
978
979
980
981



982

983 **Figure 1.** Comparison of full disk CBH results retrieved by the four-independent
984 algorithms at 02:00 UTC on January 1, 2017. (a) GEO IDPS algorithm, (b) GEO
985 Clouds from AVHRR Extended (CLAVR-x) algorithm, (c) machine-learning
986 (ML)-based (RF, random forest) VIS+IR algorithm and (d) ML-based (RF) IR-single
987 algorithm.

988

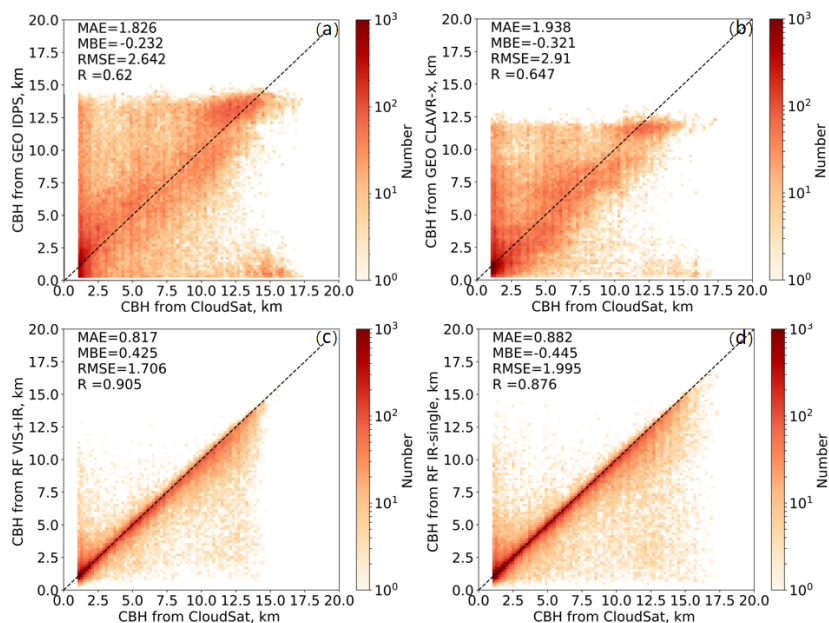
989

990

991

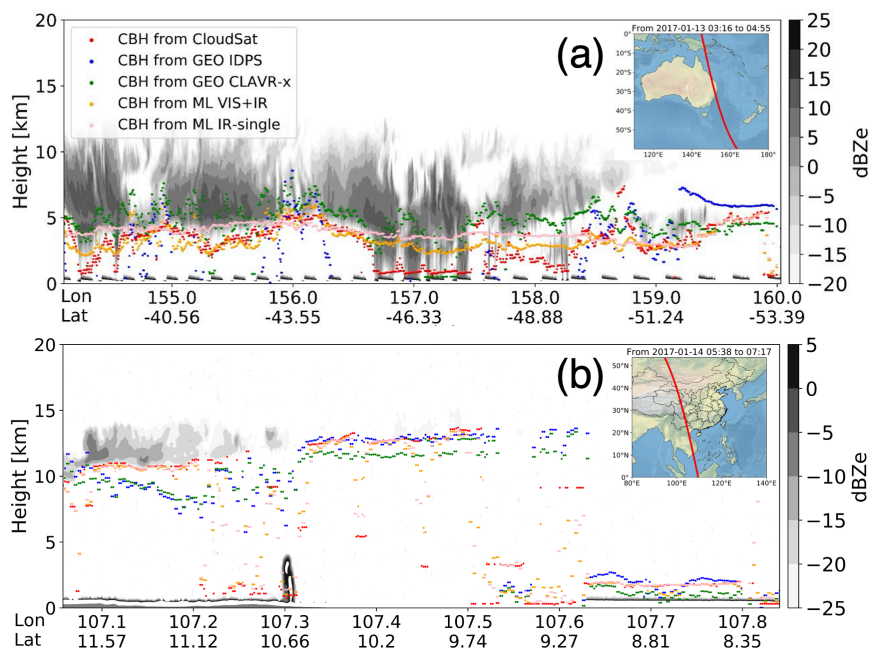
992

993



994
995 **Figure 2.** Density distributions of CBHs retrieved from (a) GEO IDPS, (b) GEO
996 CLAVR-x, (c) VIS+IR and (d) IR-single algorithms compared with the CBHs from
997 the joint CloudSat/CALIPSO product (taken as true values) in 2017. The mean
998 absolute error (MAE), mean bias error (MBE), root mean square error (RMSE) and R
999 are listed in each subfigure where the difference exceeds the 95% significance level (p
1000 < 0.05) according to the Pearson's χ^2 test.

1001
1002
1003
1004
1005
1006
1007
1008
1009
1010
1011
1012
1013



1014

1015 **Figure 3.** Inter-comparisons of CBH products retrieved by CloudSat (red solid circle),
1016 the GEO IDPS algorithm (blue solid circle), the GEO CLAVR-x (green solid circle),
1017 the ML-based VIS+IR model algorithm (orange solid circle), and the ML-based
1018 IR-single model algorithm (pink solid circle) at (a) 03:16–04:55 UTC on January 13,
1019 2017 (a) and (b) 05:38–07:17 UTC on January 14, 2017. The black and gray colormap
1020 represents the matched CloudSat radar reflectivity.

1021

1022

1023

1024

1025

1026

1027

1028

1029

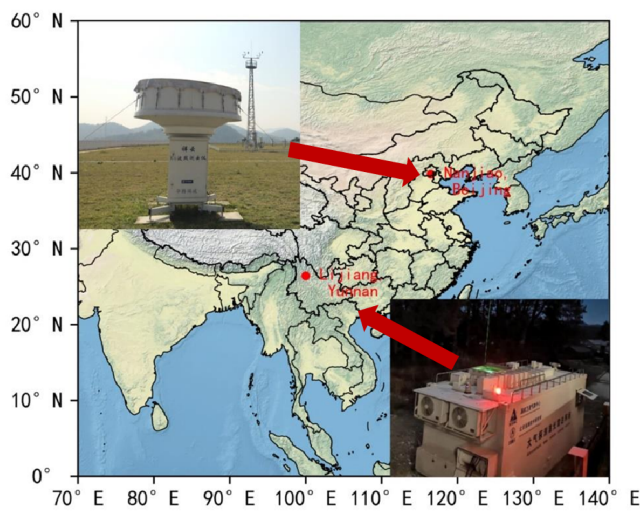
1030

1031

1032



1033



1034

1035 **Figure 4.** Geographical locations and photos of lidar and cloud radar at Yunnan
1036 Lijiang and Beijing Nanjiao stations.

1037

1038

1039

1040

1041

1042

1043

1044

1045

1046

1047

1048

1049

1050

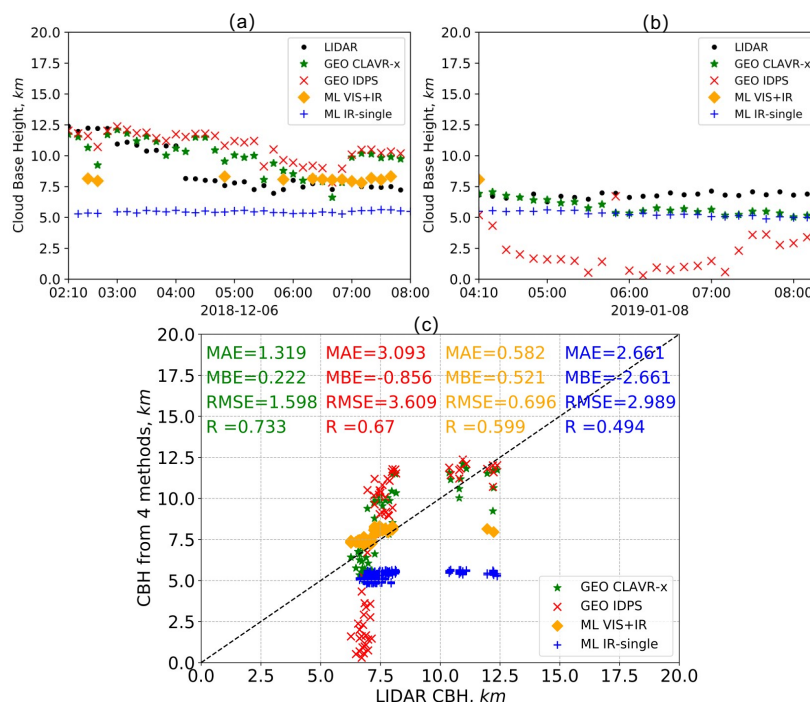
1051

1052

1053

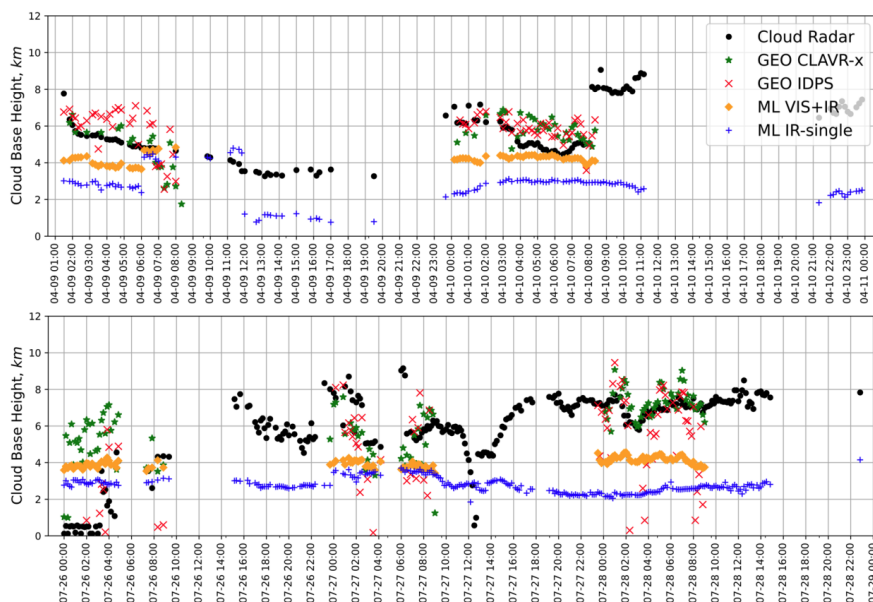
1054

1055



1056
 1057 **Figure 5.** Comparisons of the CBHs from the ground-based lidar measurements
 1058 (black solid circle) at Yunnan Lijiang station and the four GEO satellite retrieval
 1059 algorithms, namely the GEO IDPS (red cross symbol), the GEO CLAVR-x (green
 1060 solid asterisk), the ML-based VIS+IR model (orange solid diamond) and the
 1061 ML-based IR-single model (blue plus sign) algorithms. Fig 6a and 6b show the time
 1062 series of CBHs from lidar and the four GEO satellite retrieval algorithms on
 1063 December 6, 2018 and January 8, 2019, respectively. Fig 6c shows the scatterplots of
 1064 CBH samples from the lidar measurements and the four retrieval algorithms.

1065
 1066
 1067
 1068
 1069
 1070
 1071



1072

1073 **Figure 6.** Same as Fig. 6, but for the CBH sample results from the cloud radar at
1074 Beijing Nanjiao station (black solid circle) on April 9–10, 2017 (top panel) and July
1075 26–28, 2017 (bottom panel).

1076

1077

1078

1079

1080

1081

1082

1083

1084

1085

1086

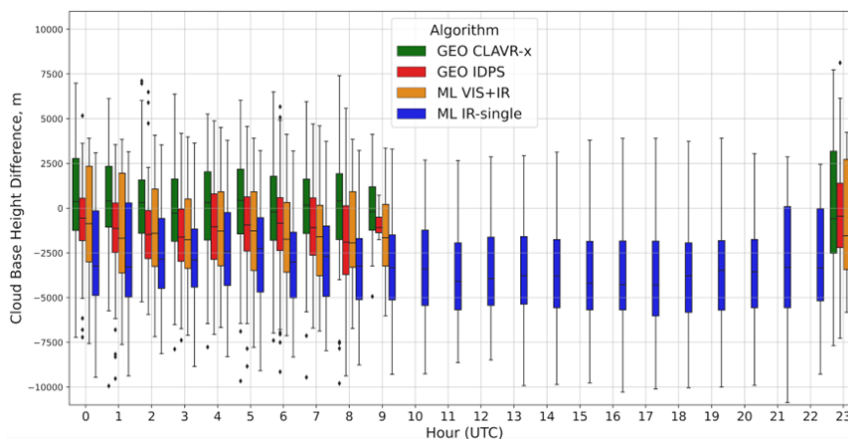
1087

1088

1089

1090

1091



1092

1093 **Figure 7.** Box plots of the hourly CBH errors of four GEO satellite retrieval
1094 algorithms (GEO IDPS, GEO CLAVR-x, ML-based VIS+IR and ML-based IR-single)
1095 relative to the CBHs from the cloud radar at Beijing Nanjiao station in 2017. The box
1096 symbols signify the 25th, 50th and 75th percentiles of errors. The most extreme
1097 sample points between the 75th and outlier, and the 25th percentiles and outliers are
1098 marked as whiskers and diamonds, respectively.

1099

1100

1101

1102

1103

1104

1105

1106

1107

1108

1109

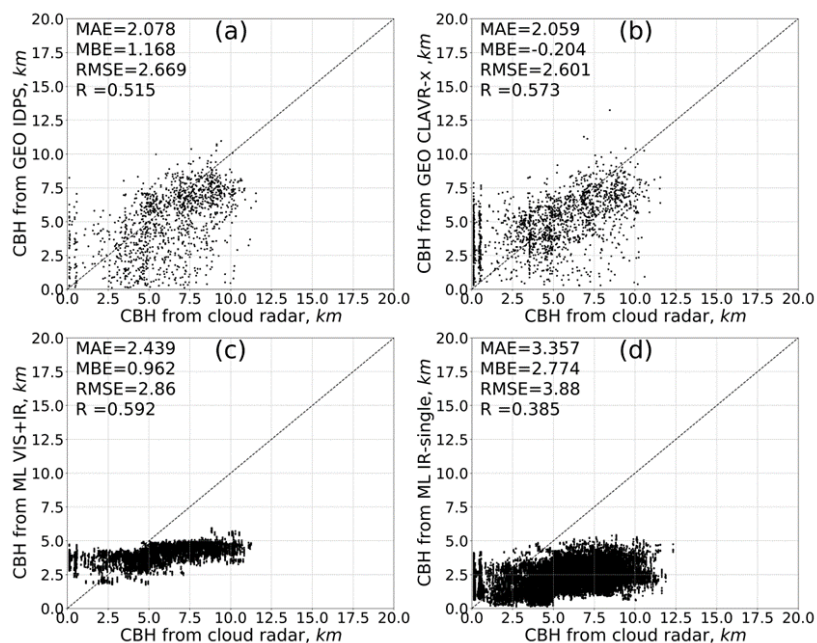
1110

1111

1112

1113

1114



1115

1116 **Figure 8.** Comparisons between the CBHs from the cloud radar at Beijing Nanjiao
1117 station and the matched CBHs from the four retrieval algorithms (GEO IDPS, GEO
1118 CLAVR-x, ML-based VIS+IR and ML-based IR-single) in 2017.

1119

1120

1121

1122

1123

1124

1125

1126

1127

1128